Ions Matter: Description of the Anomalous Electronic Behavior in Methylammonium Lead Halide Perovskite Devices

*Onkar S. Game, Gabriel J. Buchsbaum, Yuanyuan Zhou, Nitin P. Padture, and Angus I. Kingon**

Carrier transport in methylammonium lead iodide ($MAPbI_3$)-based hybrid organic–inorganic perovskites (HOIPs) is obscured by vacancy-mediated ion migration. Thus, the nature of migrating species (cation/anion) and their effect on electronic transport in $MAPbI_3$ has remained controversial. Temperature-dependent pulsed voltage–current measurements of $MAPbI_3$ thin films are performed under dark conditions, designed to decouple ion-migration/accumulation and electronic transport. Measurement conditions (electric-field history and scan rate) are shown to affect the electronic transport in $MAPbI_3$ thin films, through a mechanism involving ion migration and accumulation at the electrode interfaces. The presence of thermally activated processes with distinct activation energies (E_a) of 0.1 ± 0.001 and 0.41 ± 0.02 eV is established, and are assigned to electromigration of iodine vacancies and methylammonium vacancies, respectively. Analysis of activation energies obtained from electronic conduction versus capacitive discharge shows that the electromigration of these ionic species is responsible for the modification of interfacial electronic properties of $MAPbI_3$, and elaborates previously unaddressed issues of "fast" and "slow" ion migration. The results demonstrate that the intrinsic behavior of $MAPbI_3$ material is responsible for the hysteresis of the solar cells, but also have implications for other HOIP-based devices, such as memristors, detectors, and energy storage devices.

1. Introduction

Perovskite solar cells (PSCs) based on hybrid organic–inorganic perovskites (HOIPs) and other optoelectronic devices have shown phenomenal progress in the past few years.[1] Despite their low processing temperatures, HOIPs show exceptional optical and electrical properties (very low trap densities,[2] strong absorption,[3] and long carrier diffusion lengths[2]), which are comparable to state-of-the-art inorganic single-crystal semiconductors such as Si and GaAs. However, there is still a lack of comprehensive understanding of several fundamental properties of HOIPs, such as existence of ferroelectricity[4] and the nature and transport of point defects in HOIPs,[5] and their relation to observation of anomalous optoelectronic behaviors, such as the so-called "giant dielectric constant,"[6] current (I)–voltage (V) hysteresis,[7] and field-/light-induced phase segregation.[8,9]

Migration of point defects in $CH_3NH_3PbI_3$ (or $MAPbI_3$) HOIP under electric field (E) has been the subject of active research recently,[10] and several reports have suggested ion migration to be one of the dominant phenomena at or near room temperature. However, there is a lack of consensus over the nature of the migrating species (cation or anion). Several experimental and theoretical[11,12] studies support migration of MA^+ cations (or V'_{MA}) as the origin of the anomalous I–V response, whereas others[7,13,14] point to I^- anion (or V_I) migration. This is further obscured by a wide spread in activation energies (E_a), ranging from 0.1 to 0.6 eV, measured experimentally[11,12,15] or predicted theoretically.[12,15] Several theoretical calculations have predicted that self-regulatory charge-compensating Schottky defects (V'_{MA} and V_I) show the lowest formation energy in $MAPbI_3$, with predicted concentration of vacancy defects reaching as high as 4%.[16,17] Interestingly, these charge-compensating donor (V_I) or acceptor (V'_{MA}) defect levels reside very close to (or within) conduction and valence bands of $MAPbI_3$, and therefore do not have detrimental effects on electronic transport via long-term trapping of photogenerated carriers.[11,18] The presence of these vacancy defects should, therefore, lead to vacancy-mediated migration of both MA^+ and I^- ions with different activation energies owing to their different sizes, lattice occupancies, and diffusion pathways. However, as mentioned earlier, these have yet to be measured. It is important to note that the experimental measurements of activation energies reported so far mostly involve temperature-dependent electronic conductivity/photoconductivity or photoluminescence (PL) decay measurements.[9,11–15,19] For instance, Yuan et al.[11] observed photovoltaic switching under low E (<0.2 V μm^{-1}) as well as high E (>0.3 V μm^{-1}) fields, which they attribute to migration and accumulation of

Dr. O. S. Game, G. J. Buchsbaum, Dr. Y. Zhou, Prof. N. P. Padture, Prof. A. I. Kingon
School of Engineering
Brown University
Providence, RI 02912, USA
E-mail: angus_kingon@brown.edu

DOI: 10.1002/adfm.201606584

© 2017 WILEY-VCH Verlag GmbH & Co. KGaA, Weinheim

"fast ions" and "slow ions," respectively. However, activation energy measurement through temperature-dependent conductivity resulted in only one value of 0.36 eV related to electromigration of "slow ions," i.e. V'_{MA} (at $E > 0.3$ V μm^{-1}). Therefore, the origins of "fast" and "slow" ion migration are still not clear.

It should be noted that when temperature-dependent measurements are used to investigate transport phenomena, nonlinear processes and multiple transporting species can complicate the interpretation. Measuring a single activation energy is not necessarily indicative that a single dominant process is in play. Therefore, if one is to understand transport mechanisms it is essential to identify conditions under which there are multiple dominant processes. Thus, typical conduction measurements can be problematic, where discharge currents can provide critical insights. To address this issue and explore exclusively the charge transport behavior in $MAPbI_3$, we adopted a simplified capacitor-like metal–semiconductor–metal (M–S–M) architecture, with fluorine-doped tin oxide (FTO) and Au as the two metal electrodes (see Figure S1, Supporting Information). All the measurements were performed under dark conditions to isolate the ionic-electronic transport in $MAPbI_3$ without being obscured by photogenerated carriers and complex device architecture with electron- and hole-selective layers. We show the presence of multiple ion-migrating species differing in activation energies through temperature-dependent capacitive discharge currents obtained in different voltage/field regimes. The migration and accumulation of these ionic species lead to modification of interfacial electronic properties of $MAPbI_3$, which are manifested in field-direction and scan-rate dependency of current–voltage (I–V) measurements. Such peculiarities in I–V measurements are also observed in $MAPbI_3$-based PSCs with electron- and hole-selective layers, which presumably have their origin in ion migration. Therefore, results obtained in this study have direct implications for PSCs. Other avenues where the results of this study are likely to be insightful are detectors (photon, X-ray, radiation), and furthermore, HOIP-based memristors that depend on ion migration for their functionality.

2. Results and Discussion

Figure 1a shows the X-ray diffraction (XRD) pattern from the $MAPbI_3$ thin film confirming a pure tetragonal phase (space group $I4/mcm$). The scanning electron microscopy (SEM) images in Figure 1b,c show a full-coverage, smooth $MAPbI_3$ thin film with an average grain size of a couple of 100 nm. Thickness of $MAPbI_3$ film was determined using a step profilometer. The film thickness was found to be in the range of ≈650–700 nm for the processing conditions mentioned in the Experimental Section.

Figure 2 shows I–V curves of the FTO–$MAPbI_3$–Au device under different scanning directions. Interestingly, the character of the I–V curve depends strongly on the direction of voltage scan. For a linear scan (Figure 2a) from +1 to −1 V, the device shows a small "hump" in the I–V curve, followed by nonlinear rectifying behavior in the negative voltage region. Figure 2b shows I–V response with cyclic voltage scan, starting and ending at +1 V. A dramatic difference in the I–V curve character can be observed for the parts of the I–V curve scanned from +1 to −1 V and then −1 to +1 V. More specifically, the magnitude of measured current for +1 V at the start of the scan and at the end of the scan differ by two orders of

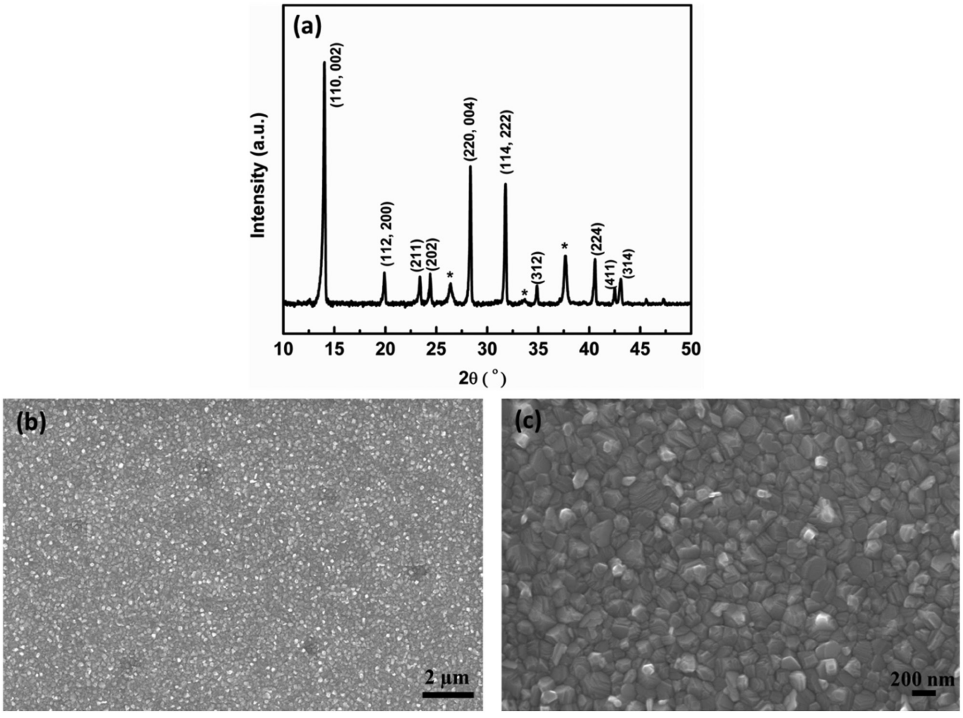

Figure 1. As-prepared $MAPbI_3$ thin film deposited using the ASE method. a) XRD pattern (* indicate reflections from the underlying FTO) and top-view SEM images at b) low magnification and c) high magnification.

© 2017 WILEY-VCH Verlag GmbH & Co. KGaA, Weinheim

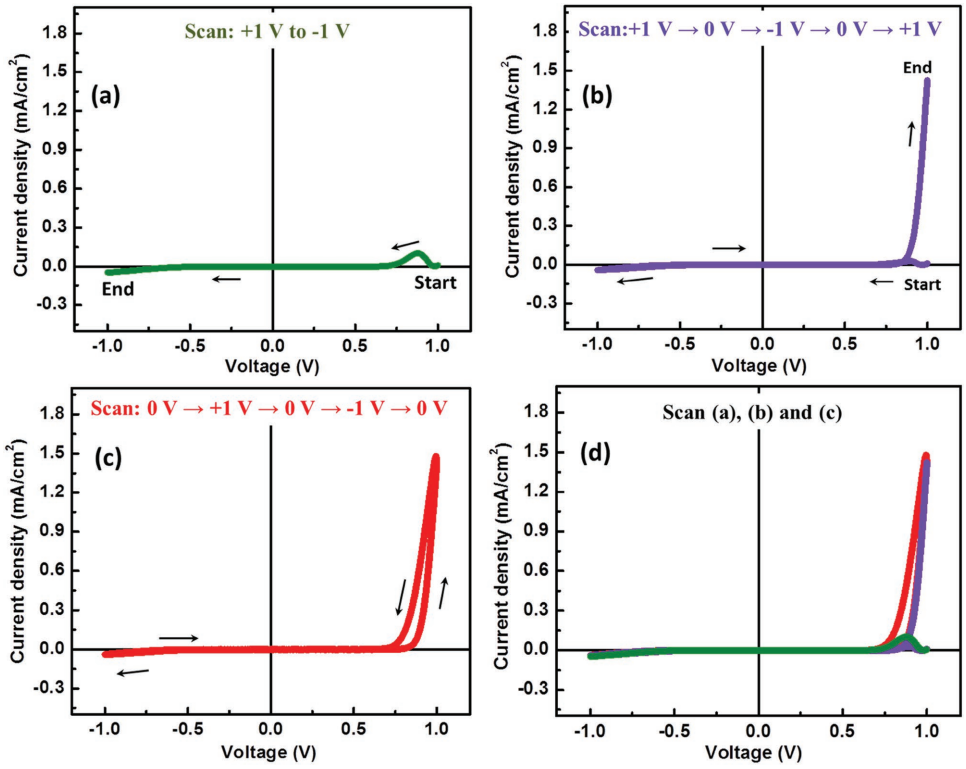

Figure 2. *I–V* curves of FTO–$MAPbI_3$–Au device under constant scan rate (20 mV s^{-1}) but different scanning directions. a) Linear scan +1 V → −1 V, b) cyclic scan +1 V → 0 V → −1 V → 0 V → +1 V, and c) cyclic scan 0 V → +1 V → 0 V → −1 V → 0 V. d) Superimposed scans from (a), (b), and (c).

magnitude. Apparent rectification in the positive voltage region is observed for scanning from −1 to +1 V. This implies that the strong rectification in positive voltage region is established with field and time.

Figure 2c shows *I–V* curve for cyclic scan with the scan sequence: 0 V → +1 V → 0 V → −1 V → 0 V. The *I–V* curve shows strong rectifying behavior in the positive voltage region, along with small hysteresis for both positive and negative biases (see also **Figure 3**a). The observed strong rectification in the positive voltage region is consistent with the part of *I–V* curve in Figure 2b when voltage is scanned from −1 to +1 V. The *I–V* curves in Figure 2a–c are superimposed in Figure 2d, which demonstrate that the observed behavior is reproducible, and that the magnitude of the current strongly depends on the direction of the voltage scan. Figure 2 clearly shows that linear *I–V*s for HOIP-based M–S–M devices can be misleading, as the magnitude of current largely depends on the scan direction. It also indicates the importance of cyclic *I–V* measurements starting from 0 V, which can capture the field-dependent dynamic rectification and hysteretic nature of the *I–V* curve.

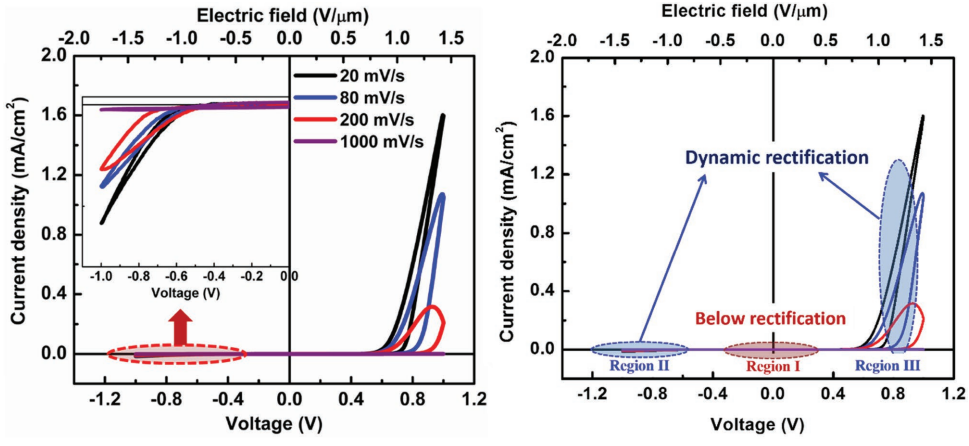

Figure 3. a) Cyclic (0 V → +1 V → 0 V → −1 V → 0 V) *I–V* curves of FTO–$MAPbI_3$–Au device at scan rates 20, 80, 200, and 1000 mV s^{-1}. Inset: Magnified view (0 to −1 V) of *I–V* curves. b) Regions of interest in *I–V* curves of FTO for temperature-dependent pulsed-voltage current measurements.

© 2017 WILEY-VCH Verlag GmbH & Co. KGaA, Weinheim

Interestingly, the recommendations for reliable photovoltaic (PV) measurements on HOIP include similar procedures due to their scan-direction and scan-rate dependent J–V response.

Figure 3a shows scan-rate dependence of the cyclic I–V responses starting from 0 V. The nature of I–V curve, which includes magnitude of current, rectification, and hysteresis, show strong dependence on the rate of voltage scan. For both positive and negative biases the magnitude of current (and hence rectification) increases with a decrease in the scan rate from 1000 to 20 mV s^{-1}. For instance, the 1000 mV s^{-1} scan shows two orders of magnitude lower current than 20 mV s^{-1} scan, with no apparent rectification for positive or negative bias. This clearly shows that the rectification under positive or negative bias has a strong scan-rate dependence.

The apparent hysteresis in the I–V curves seem to decrease with a decrease in the scan rate, which agrees well with the reported trend in hysteresis for PSCs containing electron- and hole-transport layers.[19,20] Importantly, the characteristic similarities in the nature of J–V curves of HOIP-based simplified M–S–M structures under dark, and complex photovoltaic devices under light, indicate that the phenomenological origins of hysteretic nature of PSC devices can be intrinsic to the HOIP layer. This further indicates that the hysteresis in PSC devices is less likely to have its origin in the ferroelectric behavior[21] or in the difference in photocarrier extraction at electron- and/or hole-transport layers.[22]

Previous reports[11,23,24] on $MAPbI_3$-based M–S–M devices mention the need for prepoling treatment (i.e., biasing the device at a certain voltage for a certain duration) to observe the diode-like rectifying nature. It is important to mention that the diode-like behavior of $MAPbI_3$-based M–S–M devices can be observed without any prepoling treatment, as we have shown in Figure 2. In addition, Figure 2 and 3 show that the observed rectification and hysteresis behaviors are dynamic in nature, i.e., these are established with voltage and time (scan rate). This behavior is dramatically different from typical inorganic-semiconductor-based junctions (p–n or Schottky), which do not show these anomalies in I–V behavior under similar conditions. Therefore, this exploration of the origin of I–V anomalies is central to the understanding of charge transport behavior in HOIPs.

The apparent similarity of the I–V curves of FTO–$MAPbI_3$–Au devices with that of resistive-switching-based memory devices[25] suggests that the possible origin of such I–V behavior is related to the migration of vacancy defects, which show strong temperature dependence. Pulsed voltage–current measurements on capacitor-like FTO–$MAPbI_3$–Au structures can be particularly useful in this context, as these help to separate electronic, ionic, and dielectric-displacement effects. Traditionally, such charge and discharge current versus time measurements under pulsed voltage, which include the charging and discharging currents, have been used to study dielectric relaxation phenomena in ceramics.[26] First, we identify three regions in the I–V curve of FTO–$MAPbI_3$–Au for temperature-dependent pulsed voltage–current measurements. As shown in Figure 3b, Region I corresponds to low voltage region (–0.2 to +0.2 V) below the onset of rectification, whereas in Region II ($V > |-0.7\ V|$) and Region III ($V > +0.7$ V), scan-rate-dependent dynamic rectification is observed.

Figure 4a shows temperature-dependent pulsed voltage–current measurements on FTO–$MAPbI_3$–Au device for applied voltages of ±0.2 V with a pulse width of ≈60 s. Upon application of ±0.2 V, a sharp rise in the dark current is observed, which, after several seconds (≈10 s) attains a stable value with the sign same as that of the applied +/− voltage. When the applied voltage is changed from ±0.2 to 0 V, a "discharge current" of opposite sign is observed, which is shown by dotted circles in Figure 4a. Under the application of electric field, a certain amount of charge is accumulated at the metal electrode interfaces to compensate the polarization of material due to electric field. Therefore, discharge pulses are expected due to the dissipation of this compensating charge upon removal of the applied field/voltage.

In summary, the presence of discharge pulses is an indication of the polarization of material, which may have its origin in intrinsic effects such as dielectric polarization or in the accumulation of charged species (defects) at blocking interfaces.

Figure 4b shows strong temperature dependence (in the range 80–300 K) of transient discharge currents obtained after the field equivalent to –0.2 V (≈ –0.3 V μm^{-1}) is removed. Integrating the discharge current over time gives the corresponding charge ($Q_{dis.}$) that has accumulated at the metal electrode–$MAPbI_3$ interface at a given temperature. As mentioned earlier, these transient discharge currents (and hence $Q_{dis.}$) may have their possible origin in dielectric polarization or capacitive effects due to ion accumulation. These two effects show characteristically different behavior as a function of temperature. For instance, if dielectric (de-)polarization is the sole contributor to Q_{dis}, then it would follow a trend similar to dielectric constant versus temperature for $MAPbI_3$, i.e., a decrease in the magnitude with rise in temperature above the first-order phase transition.[27] Figure 4c shows the plot of Q_{dis}. versus temperature obtained after integration of discharge currents in Figure 4b for respective temperatures. Interestingly, $Q_{dis.}$ for –0.2 V square-pulse apparently shows exponential dependence on temperature, which therefore excludes field-induced dielectric polarization as a dominant phenomenon for temperatures above 160 K. This is further supported by erroneously large dielectric constant ($k > 2700$) obtained by substitution of measured $Q_{dis.}$ at 300 K in parallel-plate capacitor approximation, $k = \frac{Qd}{\varepsilon_0 AV}$, where $d = 0.7$ μm, $Q_{dis.} = Q/A = 0.69$ μC cm^{-2}, $V =$ 0.2 V, and ε_0 is permittivity of free space. Such giant "dielectric constant" at 300 K in $MAPbI_3$ have been associated with its lossy dielectric nature arising from a large concentration of charged point defects.[6,28] Therefore, for $T > 180$ K, the exponential variation of $Q_{dis.}$ with temperature and the high interface charge density, leading to the giant "dielectric constant" indicates that charged-defect migration and accumulation is the dominant phenomenon for $T > 180$ K. However, for temperatures below the first-order tetragonal-to-orthorhombic phase transition in $MAPbI_3$ ($T < 160$ K) the $Q_{dis.}$ shows little variation with temperature. It also shows an order-of-magnitude (×25) lower charge than at room temperature. This suggests that for $T < 160$ K, dielectric polarization is the dominant contributor to Q_{dis}.

The exponential dependence of $Q_{dis.}$ with temperature suggests that the process responsible for accumulation of this

© 2017 WILEY-VCH Verlag GmbH & Co. KGaA, Weinheim

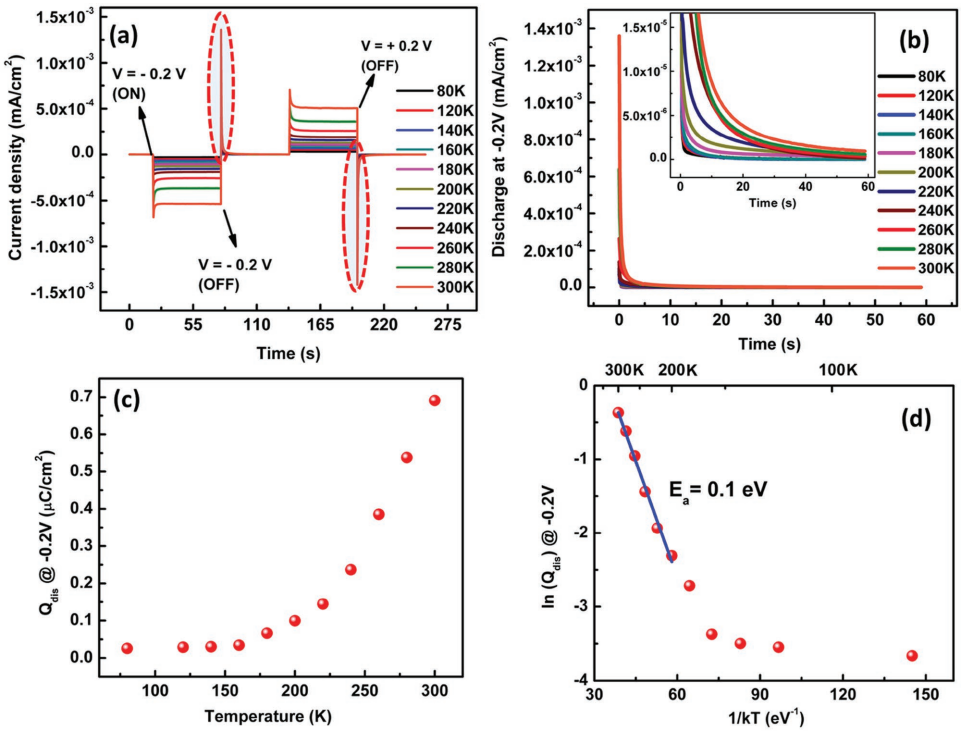

Figure 4. a) Temperature-dependent current versus time profiles of FTO–$MAPbI_3$–Au device under applied voltage pulses of ±0.2 V. Circled region shows the discharge currents (of opposite sign) after the applied voltage (±0.2 V) is removed. b) Temperature-dependent discharge currents for –0.2 V pulse plotted on time scale staring from 0 s. Inset: magnified view of discharge currents at low temperature. c) Charge ($Q_{dis.}$) obtained after integration of temperature-dependent discharge pulses in (b). d) Arrhenius representation of $Q_{dis.}$ obtained from –0.2 V pulse.

charge is thermally activated, which can be expressed using the Arrhenius equation $\frac{Q}{Q_0} = e^{\left(\frac{E_a}{kT}\right)}$, where E_a is the activation energy for the migration of charged species, k is the Boltzmann constant, and Q_0 is the pre-exponential factor. The Arrhenius plot of $\ln(Q_{dis.})$ versus $1/kT$ in Figure 4d clearly shows linear region for $T > 180$ K, which on linear fitting gives an activation E_a of 0.104 ± 0.004 eV. The analysis of discharge currents (or $Q_{dis.}$) for +0.2 V shows similar thermally activated process, with E_a of 0.103 ± 0.001 eV. This establishes that $MAPbI_3$ can show migration and accumulation of charged species under a small field ($E \approx 0.13$ V μm^{-1}) with low activation energy of $E_a \approx 0.1$ eV. Such migration of charged species under low field is in accordance with a previous observation by Yuan et al.,[11] where the charged species moving under low and high electric fields were termed as "fast ions" and "slow ions," respectively. That study did not identify the origin of these "fast ions" and "slow ions." Furthermore, activation energies derived from electronic conductivities fail to distinguish these processes. Therefore, the study of temperature-dependent discharge pulses under different applied electric field is particularly useful because of their direct association with the migrating species.

In order to gain further insights into the influence of higher electric field, and hence possible origins of dynamic rectification, we carried out similar pulsed voltage–current measurements at ±0.8 V (i.e., Region II and III in Figure 3b). The temperature-dependent current versus time profile for applied square pulse of –0.8 V in **Figure 5**a clearly shows a dramatic difference as compared to the –0.2 V case in Figure 4a. The current for –0.8 V applied potential is two orders-of-magnitude higher than that for –0.2 V, which is in accordance with the observed dynamic rectification at –0.8 V. Figure 5a,b shows strong temperature dependence of discharge pulses obtained after switching off the applied voltage of –0.8 V. Figure 5c shows the plot of $Q_{dis.}$ obtained after time integration of discharge pulses at –0.8 V ($Q_{dis.}$ for –0.2 V is plotted for comparison). Considering the capacitive nature of the M–S–M device architecture, application of higher voltage/field at a particular temperature is expected to increase linearly the magnitude of accumulated charged species ($Q_{dis.} = CV$). In such a case, the $Q_{dis.}$ versus T plot for –0.8 V should be parallel to that of –0.2 V, differing only in magnitude.

However, the observed $Q_{dis.}$ versus T plot for –0.8 V shows a dramatic difference for $T > 250$ K, thus implying the presence of an additional activated process. This is confirmed by comparison of the Arrhenius plot of $Q_{dis.}$ for –0.8 and –0.2 V in Figure 5d. As expected, Arrhenius representation of $Q_{dis.}$ for –0.8 V shows the first activation process for $T > 160$ K with the same $E_a = 0.104 \pm 0.005$ eV as observed for –0.2 V. This is evident from the parallel nature of the linear fits to Arrhenius plots for –0.8 and –0.2 V, but for $T > 250$ K the plot of $\ln(Q_{dis.})$ versus $1/kT$ for –0.8 V deviates from first linear region (E_a = 0.1 eV) to another linear region with a $E_a = 0.41 \pm 0.022$ eV, consistent with second activated process which starts at higher temperatures ($T > 250$ K) and fields. Therefore, the indication of two thermally activated processes with considerably different activation energies ($E_a \approx 0.1$ and ≈0.41 eV) implies migration and accumulation of two different species, which Yuan et al.[10,11] termed as "fast ions" and "slow ions," respectively.

© 2017 WILEY-VCH Verlag GmbH & Co. KGaA, Weinheim

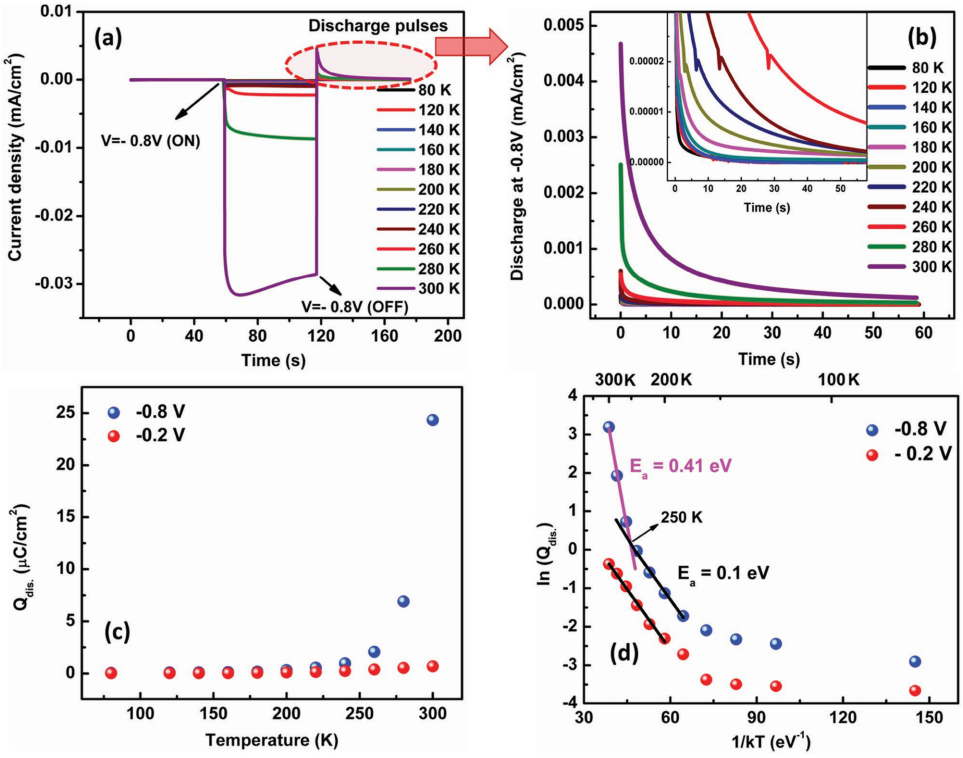

Figure 5. a) Temperature-dependent current density versus time profiles of FTO–$MAPbI_3$–Au device under an applied voltage pulse of –0.8 V. Circled region shows the discharge currents (positive) after the applied voltage (–0.8 V) is removed. b) Temperature-dependent discharge currents for –0.8 V pulse plotted on time scale staring from 0 s. Inset: magnified view of discharge currents at low temperature. c) $Q_{dis.}$ obtained after integration of temperature-dependent discharge pulses in (b). d) Arrhenius representation of $Q_{dis.}$ obtained from –0.8 V pulse (–2 V pulse data included for comparison).

Figure S2,b (Supporting Information) allows us to explain the advantage of analyzing the temperature dependence of discharge pulses (or $Q_{dis.}$) rather than the temperature dependence of current (or conductivity). In Figure S2b (Supporting Information), a stabilized current at –0.8 V is plotted in the Arrhenius representation ($\ln(I)$ vs $1/kT$), which shows two linear regions with activation energies $E_a = 0.42 \pm 0.002$ eV and $E_a = 0.027 \pm 0.003$ eV, with the transition temperature around 240 K. It is important to re-emphasize that the two electrodes (FTO and Au) used in the current device serve the purpose of blocking ions at respective interfaces, therefore, the steady-state currents observed under –0.8 V applied potential must be electronic with no contributions from ionic conductivity. Thus, the activation energy of 27 meV observed for temperature range from 80 to 240 K can be assigned to electronic transport in $MAPbI_3$. This is in accordance with previously reported experimental values[11] and also theoretical predictions[29] that I^-, $CH_3NH_3^+$, and Pb^{2+} vacancies act as shallow donor and acceptor levels with energy depth less than 50 meV. Interestingly, the activation energy $E_a = 0.42$ eV and the corresponding transition temperature of 240 K agrees well with values calculated from the discharge plots in Figure 5d. However, the smaller activation energy of 0.1 eV obtained from the $\ln(Q_{dis.})$ versus $1/kT$ plot is not observed in the $\ln(I)$ versus $1/kT$ plot for –0.8 V. This clearly indicates the following:

1. Since $Q_{dis.}$ derived from discharge pulses has direct correlation with the accumulated charge at interfaces, its Arrhenius representation can resolve the activation energies arising due to the migration of different ionic species differing in activation energy. This is because the discharge currents exclude leakage currents, whereas the Arrhenius plots of conductivity include the leakage currents that are controlled by an interdependent, nonlinear relation between charge accumulation and changes in the interfacial electrical properties.
2. The comparable values of activation energies, i.e., $E_a = 0.41$ eV from $\ln(Q_{dis.})$ versus $1/kT$ (Figure 5d) and $E_a = 0.42$ eV from $\ln(I)$ versus $1/kT$ (Figure S2b, Supporting Information) implies that modification of electronic properties at HOIP–metal interface is more dramatic after migration and accumulation of "slow ions," although the migration of the "fast ions" start under lower fields. Additionally, the comparable values of activation energies ($E_a \approx 0.4$ eV) derived from discharge curves (Figure 5d) and steady-state currents (Figure S2b, Supporting Information) implies that the charged species that are accumulating at the electrode interfaces are also responsible for the modification of the electronic character at the two interfaces, which results in the dynamic rectification.

Hoque et al.[30] observed a decrease in activation energy (0.73 to 0.51 eV) of ion migration in $MAPbI_3$ solar cells around 320 K, which roughly falls in the temperature regime of tetragonal-to-cubic phase transition. This decrease was tentatively assigned to the difference in the vacancy-hopping mechanism arising due to crystal symmetry change, thus leading to different activation barriers. In the present study, the transition

© 2017 WILEY-VCH Verlag GmbH & Co. KGaA, Weinheim

from E_a = 0.1 eV to E_a = 0.41 eV occurs around 250 K, which does not coincide with the T_C for the orthorhombic-to-tetragonal or tetragonal-to-cubic phase transitions, and which therefore excludes the possibility of change in activation energy due to crystal symmetry change. However, the onset of the lower-activation ion migration process (characterized by the change from ≈27 meV to 0.1 eV) roughly coincides with the first-order orthorhombic-to-tetragonal phase transition around 160 K, which likely points toward a structural mediation of the migration mechanism, such as that proposed by Hoque et al.[30]

Interestingly, the values of activation energies (≈0.42 eV and ≈27 meV) observed from ln(I) versus $1/kT$ are in accordance with the activation energies measured by Yuan et al.[11] of ≈0.36 eV and ≈35 meV using temperature-dependent conductivity of lateral PV devices. In the same report they showed convincing evidence of electromigration of MA^+ ions using photothermal-induced resonance spectroscopy studies for field $E > 0.5$ V μm^{-1}. Therefore, it is reasonable to assign the higher value of activation energy (E_a = 0.41 eV) observed in this study to V'_{MA}-mediated diffusion of MA^+ ions. This is also in accordance with the theoretical calculation of activation energies for MA^+ (V'_{MA}) by Haruyama et al.[31] and Azpiroz et al.,[12] who assigned the typical slow time scales (≈10 s) of photoresponse and hysteresis to migration of V'_{MA} (E_a = 0.5–0.6 eV). Also, according to those reports the values of E_a for $V_I^{\cdot}$ migration should lie in the range of 0.1–0.2 eV. Theoretical calculations of activation energies for defect migration in $MAPbI_3$ by several research groups have led to a large spread of possible values corresponding to migration of different species. However, there is a consensus on diffusion of $V_I^{\cdot}$ being the most facile process. Therefore, the low value of activation energy E_a = 0.1 eV obtained from ln($Q_{dis.}$) versus $1/kT$ for −0.8 or −0.2 V can be assigned to migration of $V_I^{\cdot}$ (or vacancy-mediated migration of I^-). This is in accordance with the recent experimental measurements of activation energies using techniques such as temperature-dependent photocurrent decays[13,32] of PSCs or photoluminescence rise times[9] of mixed-halide HOIPs. Considering the lower activation energy of $V_I^{\cdot}$ than V'_{MA}, those techniques are more likely to be sensitive to the migration of $V_I^{\cdot}$ than V'_{MA}. Interestingly, the measured activation energy E_a = 0.1 eV is also in perfect agreement with the predicted activation energy of $V_I^{\cdot}$ migration using molecular simulation dynamics by Mattoni and co-workers[33]

Egger et al.[34] recently predicted proton migration as one of the possibilities in HOIPs. There are two possible scenarios in which free protons can be formed within $MAPbI_3$: (a) deprotonation[34] of $CH_3NH_3^+$ with the escape of CH_3NH_2 or (b) adsorption of water molecule[35] on the $MAPbI_3$ surface. Based on the equilibrium constant of deprotonation reaction ($CH_3NH_3^+ \leftrightarrow CH_3NH_2 + H^+$), the maximum concentration of free H^+ ions at 300 K is predicted to be 10^{11} cm^{-3}.[17] Considering the device dimensions in this study (≈700 nm thickness), the estimated maximum areal charge density of H^+ would be 1.12×10^{-6} μC cm^{-2}, whereas the observed accumulated charge density, even at low potentials (0.2 V) at 300 K, is ≈0.7 μC cm^{-2}, five orders of magnitude higher than the estimated H^+ in scenario (a). Therefore, deprotonation of $CH_3NH_3^+$ is an unlikely contributor to ion migration observed in this study. Alternatively, Müller et al.[35] reported that $MAPbI_3$ surface can rapidly (within seconds) adsorb water molecules even under low humidity conditions. However, based on infrared spectroscopy, they also observed that on exposing films to vacuum the effect could be fully reversed. In our study, all the device processing is performed in a nitrogen-filled glovebox (H_2O <1 ppm) and for measurements, the films were transferred to a vacuum cryostat, and all the measurements were performed under vacuum (≈10^{-3} Torr). Therefore, the likely effects of adsorbed water are expected to be minimal (although cannot be completely ruled out).

Huang and co-workers[36] reported that grain boundaries can be dominant pathways for ion migration in HOIPs, which might lead to differences in the measured values of activation energies. However, the presence of rectifying behavior in both fine- and coarse-grained $MAPbI_3$ devices is indicative of the modified interfaces due to ion migration and accumulation, although some differences in hysteretic behavior at different scan rates may be expected for coarse- versus fine-grained films.

We now turn our attention to Region III in Figure 3b, which shows higher hysteresis and dynamic rectification as compared to Region II. **Figure 6**a shows the temperature-dependent current versus time profiles for +0.8 V applied pulse with the discharge pulses shown in the inset. The room-temperature magnitude of steady-state current under +0.8 V is larger than corresponding magnitude for −0.8 V. This is in accordance with larger dynamic rectification observed for positive potentials.

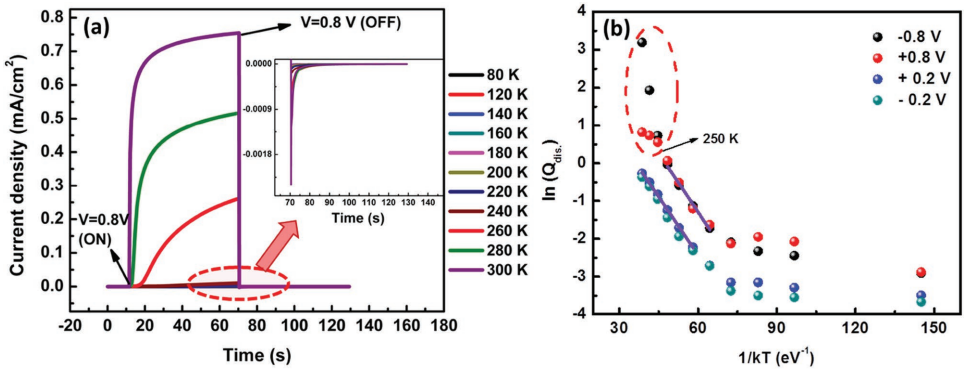

Figure 6. a) Temperature-dependent current versus time profiles of FTO–$MAPbI_3$–Au device under applied voltage pulse of +0.8 V. Circled region shows the discharge currents (negative) after the applied voltage (+0.8 V) is removed. b) Arrhenius representation of $Q_{dis.}$ obtained from +0.8 V pulse (±0.2 V and −0.8 V pulse data included for comparison).

© 2017 WILEY-VCH Verlag GmbH & Co. KGaA, Weinheim

Temperature dependence of charge ($Q_{dis.}$) obtained after time integration of discharge pulses for +0.8 V is plotted against $1/kT$ in Figure 6b. Corresponding data for ±0.2 V and −0.8 V are also plotted for reference. For temperatures $160 < T < 240$ K, $\ln(Q_{dis.})$ versus $1/kT$ plot at +0.8 V follows the same trend as −0.8 V, implying the presence of first thermally activated process with $E_a = 0.11 \pm 0.008$ eV, which is previously assigned to $V_I^{\cdot}$ migration. Deviation from the first thermally-activated process is also observed at the same transition temperature of $T \approx 240$ K, which indicates that the transition is related to electromigration of V'_{MA}, as discussed earlier. Interestingly, for $T > 240$ K the absolute magnitudes of $Q_{dis.}$ are smaller than the values observed for −0.8 V, indicating the presence of asymmetry in the accumulation of charge at the top (Au–$MAPbI_3$) and the bottom (FTO–$MAPbI_3$) interface. The other aspects of asymmetry at the two interfaces can also be seen in the current-rise with time under applied bias and decay time of the discharge pulse. Figure S3a (Supporting Information) shows that after application of +0.8 V, it takes almost 30–40 s for the current to attain maximum value, as opposed to 10 s for −0.8 V. Also, the decay time of discharge pulse for +0.8 V is faster than −0.8 V as shown in Figure S3b (Supporting Information).

As mentioned earlier, the small work-function difference between FTO and Au cannot explain the asymmetry in the magnitudes of the currents, which also depend on sweep rate and scan direction. Interestingly, previous reports[23] on perovskite-based M–S–M devices made with nearly the same work-function electrodes such as PEDOT:PSS and Au also show asymmetry in the magnitudes of the currents for positive and negative applied biases. This was attributed to a difference in the interfacial electronic structure at the two interfaces, viz., PEDOT:PSS–$MAPbI_3$ and $MAPbI_3$–Au interface. A possible origin of such asymmetry may lie in the difference in defect concentration at the top interface ($MAPbI_3$–Au) and the buried interface (FTO–$MAPbI_3$). This can be particularly important considering the low formation energy of vacancy defects in HOIPs, which make free surfaces (and grain boundaries) more susceptible to defects than bulk. Very recently, Komesu et al.[37] showed, using angle-resolved photoemission spectroscopy and inverse photoemission spectroscopy, that surfaces of $MAPbBr_3$ HOIP single crystals have higher vacancy concentration than the bulk, which results in n-type character at the surface instead of the expected p-type character. In another study, Wu et al.[38] also observed two orders-of-magnitude higher surface defect density compared to bulk for both $MAPbI_3$ and $MAPbBr_3$ single crystals. Therefore, such asymmetry is likely to influence the I–V curves and temperature-dependent pulsed voltage–current measurements, which have their origin in the vacancy-mediated migration and accumulation of ions at the top and the bottom interfaces.

We postulate the origin of such asymmetry in the relatively higher concentration of charged Schottky pair defects ($V_I^{\cdot}$ and V'_{MA}) in the top interface (and possibly at the grain boundaries) as compared to bulk of the film (and interior of grains). This speculation is based on the observed n-type character of free surfaces in $MAPbI_3$ and $MAPbBr_3$,[37,38] which is attributed to high surface vacancy defects. In our measurement system, "high" and "low" of the power-source unit are connected to Au and FTO, respectively. Therefore, under positive bias, $V_I^{\cdot}$ drift away whereas V'_{MA} drift toward the $MAPbI_3$–Au interface. When $V > +0.4$ V, V'_{MA} begin migrating from the bulk to the $MAPbI_3$–Au interface. However, their accumulation is opposed by the high concentration of vacancy defects (V'_{MA}) already present near the interface, leading to lower accumulation of V'_{MA} as compared to the −0.8 V case. This explains the low magnitude of $Q_{dis.}$ observed at +0.8 V as compared to that at −0.8 V. Also, the Coulombic opposition to accumulation of V'_{MA} by high concentration of vacancies already present at the $MAPbI_3$–Au interface explains the longer time (≈40 s) needed for the modification of the electronic properties near this interface. This higher Coulombic repulsion also explains the faster decay times at +0.8 V as compared with that at −0.8 V. Also, accumulation of V'_{MA} under +0.8 V bias makes $MAPbI_3$–Au interface rich in V'_{MA} as compared to $V_I^{\cdot}$, which leads to a change in its electronic character from n-type (or intrinsic) to p-type, thereby reducing the barrier for current flow,[10,11,23,24] which explains the higher current in the +0.8 V case. Under low applied potentials ($V < 0.3$ V), the magnitude of fields are only sufficient to start migration of $V_I^{\cdot}$ due to their low activation energy. However, these fields ($V < 0.3$ V) might not be sufficient to achieve high depletion of $V_I^{\cdot}$ to result in V'_{MA}-rich interfacial regions, and hence nonrectifying character is observed for lower potentials. Direct verification of the asymmetry in the spatial distribution of the defects at the top and bottom interfaces await electron microscopy and spectroscopy characterization, but that is notoriously difficult due to the extreme sensitivity of HOIPs to electron-beam damage.

The results obtained from temperature-dependent pulsed current–voltage measurements on FTO–$MAPbI_3$–Au (M–S–M) device can offer useful insights on the mechanism of hysteresis in PSC architectures with electron and hole transport layers. Observation of scan-rate-dependent hysteretic or memristic behavior of FTO–$MAPbI_3$–Au device under dark conditions clearly implies that the origin of hysteresis in PSCs is most likely to be intrinsic to the HOIP layer rather than differential charge extraction rates of electron- and hole-transport layers under illumination. The temperature-dependent pulsed voltage–current measurement on M–S–M devices showed accumulation of large amounts of interfacial charge, which shows strong temperature dependence. At 300 K, the magnitude of this interfacial charge measured here is similar to what is observed on completed PSCs,[39] thus supporting the argument that ion migration and accumulation takes place under device operating conditions. The temperature dependence analysis in the present study points toward migration of both anionic (V'_{MA}) and cationic ($V_I^{\cdot}$) species with different activation energy. It is this migration and accumulation at the respective interfaces, which lead to modification of the electronic character of the interface (as shown in Figures 2 and 3), and is, therefore, the most likely cause of the hysteretic effects in PSCs.

3. Conclusion

In summary, charge transport behavior in $MAPbI_3$ HOIP thin films was measured under dark conditions using a simplified capacitor-like M–S–M architecture with FTO and Au as the two metal electrodes. Dark I–V measurements on FTO–$MAPbI_3$–Au devices show several unusual features, e.g., dependence of the

© 2017 WILEY-VCH Verlag GmbH & Co. KGaA, Weinheim

magnitude of the current on scan direction and scan rate, which we call "dynamic" rectification. In order to analyze the complex nature of charge transport (electronic/ionic/electronic-ionic) pulsed voltage–current measurements schemes were carefully designed, which can decouple the ion-migration and accumulation from electronic transport. Using temperature-dependent capacitive discharge currents under different voltage regimes, we clearly establish the presence of two thermally activated processes with different activation energies, viz., $E_a = 0.1$ and 0.41 eV, which are attributed to electromigration of $V_I^{\cdot}$ and V'_{MA}, respectively. At room temperature, the electromigration and accumulation of these species initiate under different field regimes—$E < 0.4$ V μm^{-1} for $V_I^{\cdot}$ and $E > 0.4$ V μm^{-1} for V'_{MA}. Most importantly, measurement of activation energy using electronic conduction versus capacitive discharge methods give comparable values ($E_a \approx 0.4$ eV). This implies that the charged species which are accumulating at the electrode interfaces are also responsible for modification of the electronic character at two interfaces resulting in the dynamic rectification. These results also provide insights into previously unaddressed issue of the observation of "fast ions" and "slow ions" in HOIPs-based switchable lateral PV devices. The origin of the asymmetry in the pulsed voltage–current measurements under opposite fields appears to be due to the presence of higher concentration vacancies at the surface (and grain boundaries) compared to the bulk. The methods developed here are generic and can be applied to other HOIPs. The methods, results, and insights presented in this study have implications not only for PSCs but also for other HOIP-based optoelectronic devices such as memristors, detectors (photons, X-rays, radiation), and energy storage devices.

4. Experimental Section

FTO substrates (Hartford Glass) of dimensions 1″ × 1″ and sheet resistance 8 Ω sq^{-1} were etched using zinc dust and dilute aqueous hydrochloric acid. Substrates were then sequentially washed using soap, deionized water, and absolute ethanol, and they were finally heated at 450 °C for 1 h to remove any surface contaminants. Before $MAPbI_3$ thin-film deposition, a part of the etched substrate was masked with Kapton tape. $MAPbI_3$ HOIP thin films were deposited using the antisolvent–solvent extraction (ASE) method reported elsewhere.[40] Briefly, 50 wt% $MAPbI_3$ solution was prepared by dissolving PbI_2 (Sigma-Aldrich 99.9995%) and MAI (Dyesol) in stoichiometric (1:1) ratio in mixed solvents of NMP:GBL (7:3 by wt). $MAPbI_3$ solution was spin-coated on cleaned FTO substrate at 2000 rpm for 20 s and immediately dipped in diethyl ether (DEE) bath for 90 s. The color of film changed from transparent to dark brown during the DEE bathing. After removing from DEE bath, the films were dried in air and heated at 100 °C for 5 min. This process resulted in $MAPbI_3$ films of thickness ≈650–700 nm, as determined by a step profilometer. All steps related to $MAPbI_3$ film preparation were performed inside an N_2-filled glovebox. The as-deposited $MAPbI_3$ thin films were characterized by XRD (D8 Discover, Bruker) using Cu Kα radiation, and by SEM (Leo, Zeiss).

Top Au contacts (80 nm) on the $MAPbI_3$ thin film were deposited using thermal evaporation under a base pressure of 10^{-6} Torr. The area of the device was defined based on overlapping geometric area of gold strip, $MAPbI_3$, and FTO. Thin Cu wires were soldered to bare FTO and top Au contact using In. A schematic diagram of FTO–$MAPbI_3$–Au device is shown in Figure S1 (Supporting Information) The device was then transferred to the cryostat chamber (VPF-100, Janis), which was evacuated continuously using a mechanical pump (pressure ≈10^{-3} Torr). Temperature was controlled using a temperature controller (335, Lakeshore). All temperature-dependent electrical measurements were performed in dark using a sourcemeter (2635A, Keithley). For all electrical measurements reported here, "high" and "low" of the sourcemeter are connected to the top Au electrode and the bottom FTO electrode, respectively. The work function of both Au top electrode and FTO bottom electrode used in the M–S–M devices is ≈5 eV.[41]

Supporting Information

Supporting Information is available from the Wiley Online Library or from the author.

Acknowledgements

The authors thank Dr. S. Kim for fruitful discussions and experimental assistance. Funding for this research was provided by the National Science Foundation (Grant No. OIA-1538893).

Received: December 13, 2016
Revised: January 30, 2017
Published online: March 15, 2017

[1] a) W. Zhang, G. E. Eperon, H. J. Snaith, *Nat. Energy* **2016**, *1*, 16048; b) S. D. Stranks, H. J. Snaith, *Nat. Nanotechnol.* **2015**, *10*, 391.
[2] D. Shi, V. Adinolfi, R. Comin, M. Yuan, E. Alarousu, A. Buin, Y. Chen, S. Hoogland, A. Rothenberger, K. Katsiev, *Science* **2015**, *347*, 519.
[3] S. De Wolf, J. Holovsky, S.-J. Moon, P. Löper, B. Niesen, M. Ledinsky, F.-J. Haug, J.-H. Yum, C. Ballif, *J. Phys. Chem. Lett.* **2014**, *5*, 1035.
[4] a) Y. Kutes, L. Ye, Y. Zhou, S. Pang, B. D. Huey, N. P. Padture, *J. Phys. Chem. Lett.* **2014**, *5*, 3335; b) S. G. Sharada, P. Mahale, B. P. Kore, S. Mukherjee, M. S. Pavan, C. De, S. Ghara, A. Sundaresan, A. Pandey, T. N. Guru Row, D. D. Sarma, *J. Phys. Chem. Lett.* **2016**, *7*, 2412.
[5] T. M. Brenner, D. A. Egger, L. Kronik, G. Hodes, D. Cahen, *Nat. Rev. Mater.* **2016**, *1*, 15007.
[6] E. J. Juarez-Perez, R. S. Sanchez, L. Badia, G. Garcia-Belmonte, Y. S. Kang, I. Mora-Sero, J. Bisquert, *J. Phys. Chem. Lett.* **2014**, *5*, 2390.
[7] H. J. Snaith, A. Abate, J. M. Ball, G. E. Eperon, T. Leijtens, N. K. Noel, S. D. Stranks, J. T.-W. Wang, K. Wojciechowski, W. Zhang, *J. Phys. Chem. Lett.* **2014**, *5*, 1511.
[8] E. T. Hoke, D. J. Slotcavage, E. R. Dohner, A. R. Bowring, H. I. Karunadasa, M. D. McGehee, *Chem. Sci.* **2015**, *6*, 613.
[9] D. W. deQuilettes, W. Zhang, V. M. Burlakov, D. J. Graham, T. Leijtens, A. Osherov, V. Bulović, H. J. Snaith, D. S. Ginger, S. D. Stranks, *Nat. Commun.* **2016**, *7*, 11683.
[10] Y. Yuan, J. Huang, *Acc. Chem. Res.* **2016**, *49*, 286.
[11] Y. Yuan, J. Chae, Y. Shao, Q. Wang, Z. Xiao, A. Centrone, J. Huang, *Adv. Energy Mater.* **2015**, *5*, 1500615.
[12] J. M. Azpiroz, E. Mosconi, J. Bisquert, F. De Angelis, *Energy Environ. Sci.* **2015**, *8*, 2118.
[13] C. Li, S. Tscheuschner, F. Paulus, P. E. Hopkinson, J. Kiessling, A. Kohler, Y. Vaynzof, S. Huettner, *Adv. Mater.* **2016**, *28*, 2446.
[14] a) S. Meloni, T. Moehl, W. Tress, M. Franckevicius, M. Saliba, Y. H. Lee, P. Gao, M. K. Nazeeruddin, S. M. Zakeeruddin, U. Rothlisberger, M. Graetzel, *Nat. Commun.* **2016**, *7*, 10334; b) G. Richardson, S. E. J. O'Kane, R. G. Niemann, T. A. Peltola, J. M. Foster, P. J. Cameron, A. B. Walker, *Energy Environ. Sci.* **2016**, *9*, 1476.

 © 2017 WILEY-VCH Verlag GmbH & Co. KGaA, Weinheim

[15] C. Eames, J. M. Frost, P. R. F. Barnes, B. C. O'Regan, A. Walsh, M. S. Islam, *Nat. Commun.* **2015**, *6*, 7497.
[16] A. Walsh, D. O. Scanlon, S. Chen, X. Gong, S. H. Wei, *Angew. Chem.* **2015**, *127*, 1811.
[17] J. M. Frost, A. Walsh, *Acc. Chem. Res.* **2016**, *49*, 528.
[18] J. Kim, S.-H. Lee, J. H. Lee, K.-H. Hong, *J. Phys. Chem. Lett.* **2014**, *5*, 1312.
[19] E. L. Unger, E. T. Hoke, C. D. Bailie, W. H. Nguyen, A. R. Bowring, T. Heumuller, M. G. Christoforo, M. D. McGehee, *Energy Environ. Sci.* **2014**, *7*, 3690.
[20] a) T. Liu, K. Chen, Q. Hu, R. Zhu, Q. Gong, *Adv. Energy Mater.* **2016**, *6*, 1600457; b) L. Meng, J. You, T.-F. Guo, Y. Yang, *Acc. Chem. Res.* **2016**, *49*, 155.
[21] J. M. Frost, K. T. Butler, A. Walsh, *APL Mater.* **2014**, *2*, 081506.
[22] Q. Jiang, L. Zhang, H. Wang, X. Yang, J. Meng, H. Liu, Z. Yin, J. Wu, X. Zhang, J. You, *Nat. Energy* **2016**, *2*, 16177.
[23] Z. Xiao, J. Huang, *Adv. Electron. Mater.* **2016**, *2*, 1600100.
[24] Z. Xiao, Y. Yuan, Y. Shao, Q. Wang, Q. Dong, C. Bi, P. Sharma, A. Gruverman, J. Huang, *Nat. Mater.* **2015**, *14*, 193.
[25] R. Waser, M. Aono, *Nat. Mater.* **2007**, *6*, 833.
[26] M. Lamhamdi, P. Pons, U. Zaghloul, L. Boudou, F. Coccetti, J. Guastavino, Y. Segui, G. Papaioannou, R. Plana, *Microelectron. Reliab.* **2008**, *48*, 1248.
[27] N. Onoda-Yamamuro, T. Matsuo, H. Suga, *J. Phys. Chem. Solids* **1992**, *53*, 935.
[28] D. P. Almond, C. R. Bowen, *J. Phys. Chem. Lett.* **2015**, *6*, 1736.
[29] a) W.-J. Yin, T. Shi, Y. Yan, *Appl. Phys. Lett.* **2014**, *104*, 063903; b) W.-J. Yin, T. Shi, Y. Yan, *Adv. Mater.* **2014**, *26*, 4653.
[30] M. N. F. Hoque, N. Islam, Z. Li, G. Ren, K. Zhu, Z. Fan, *ChemSusChem* **2016**, *9*, 2692.
[31] J. Haruyama, K. Sodeyama, L. Han, Y. Tateyama, *J. Am. Chem. Soc.* **2015**, *137*, 10048.
[32] H. Yu, H. Lu, F. Xie, S. Zhou, N. Zhao, *Adv. Funct. Mater.* **2016**, *26*, 1411.
[33] P. Delugas, C. Caddeo, A. Filippetti, A. Mattoni, *J. Phys. Chem. Lett.* **2016**, *7*, 2356.
[34] D. A. Egger, L. Kronik, A. M. Rappe, *Angew. Chem., Int. Ed.* **2015**, *54*, 12437.
[35] C. Müller, T. Glaser, M. Plogmeyer, M. Sendner, S. Döring, A. A. Bakulin, C. Brzuska, R. Scheer, M. S. Pshenichnikov, W. Kowalsky, A. Pucci, R. Lovrinčić, *Chem. Mater.* **2015**, *27*, 7835.
[36] Y. Shao, Y. Fang, T. Li, Q. Wang, Q. Dong, Y. Deng, Y. Yuan, H. Wei, M. Wang, A. Gruverman, J. Shield, J. Huang, *Energy Environ. Sci.* **2016**, *9*, 1752.
[37] T. Komesu, X. Huang, T. R. Paudel, Y. B. Losovyj, X. Zhang, E. F. Schwier, Y. Kojima, M. Zheng, H. Iwasawa, K. Shimada, M. I. Saidaminov, D. Shi, A. L. Abdelhady, O. M. Bakr, S. Dong, E. Y. Tsymbal, P. A. Dowben, *J. Phys. Chem. C* **2016**, *120*, 21710.
[38] B. Wu, H. T. Nguyen, Z. Ku, G. Han, D. Giovanni, N. Mathews, H. J. Fan, T. C. Sum, *Adv. Energy Mater.* **2016**, *6*, 1600551.
[39] H. Zhang, C. Liang, Y. Zhao, M. Sun, H. Liu, J. Liang, D. Li, F. Zhang, Z. He, *Phys. Chem. Chem. Phys* **2015**, *17*, 9613.
[40] Y. Zhou, M. Yang, W. Wu, A. L. Vasiliev, K. Zhu, N. P. Padture, *J. Mater. Chem. A* **2015**, *3*, 8178.
[41] M. G. Helander, M. T. Greiner, Z. B. Wang, W. M. Tang, Z. H. Lu, *J. Vac. Sci. Technol., A* **2011**, *29*, 011019.

© 2017 WILEY-VCH Verlag GmbH & Co. KGaA, Weinheim